



A highly selective tin-copper bimetallic electrocatalyst for the electrochemical reduction of aqueous CO₂ to formate

Xingxing Jiang^a, Xikui Wang^a, Zhenjie Liu^b, Qinglong Wang^a, Xin Xiao^a, Haiping Pan^a, Man Li^a, Jiawei Wang^b, Yong Shao^c, Zhangquan Peng^b, Yan Shen^{a,*}, Mingkui Wang^a

^a Wuhan National Laboratory for Optoelectronics, Huazhong University of Science and Technology, Wuhan, 430074, PR China

^b State Key Laboratory of Electroanalytical Chemistry, Changchun Institute of Applied Chemistry, Chinese Academy of Science, Changchun, 130022, PR China

^c Key Laboratory of the Ministry of Education for Advanced Catalysis Materials, Zhejiang Normal University, Jinhua, 321004, PR China

ARTICLE INFO

Keywords:

Carbon dioxide reduction
Cu-Sn bimetallic catalyst
Interface electronic regulation
In-situ Raman spectroscopy
Density functional theory

ABSTRACT

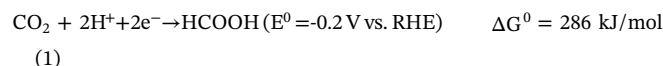
Electrochemical reduction of CO₂ is promising for mitigating the excessive CO₂ emission. However, the low efficiency and poor selectivity for targeted products block the practical application of most conventional electrocatalysts. Here, we developed an electronic regulation Cu embedded into Sn nanoparticles heterogeneous bimetallic catalyst, with high catalytic activity and selectivity for electrochemical reduction of CO₂. The excellent performance of high activity is mainly due to the appearance of abundant Sn-Cu interfaces after Cu embedded into Sn nanoparticles. XPS characterization indicates that the atomic Sn electronic structure of the bimetallic catalyst was significantly regulated by deposited Cu atoms. DFT calculations in combination with In-situ Raman spectroscopy characterization on CO₂ reduction process further indicates that the electronic regulation of bimetallic catalyst facilitates the formation of key intermediate HCOO⁻ followed by the generation of formate with high selectivity. The present design provides a method to prepare bimetallic catalyst with high catalytic performance.

1. Introduction

A great deal of attention has been paid to search technologies for carbon dioxide (CO₂) conversion and utilization to mitigate excessive emission of CO₂ and the energy crisis [1–4]. Among various available proposals to achieve this goal, electrochemical CO₂ reduction (ECR) has become an emerging technique that aims not only to reduce the levels of CO₂ but also to convert this undesirable molecule into value-added chemical products. Before it comes into true, however, challenges still remain to be addressed despite the involved significance of CO₂ electrochemical reduction in the field of energy and environment concerns. CO₂ is a chemical stable molecule owing to its lineal molecular structure and chemical inertness. So, electrochemically breaking the C=O bond of CO₂ requires a high activation energy and thus significant overpotentials [5–7]. The thermodynamic and slow kinetics together with accompanied side reaction constitute the major barriers for efficient CO₂ reduction. A variety of products such as carbon monoxide, formate, methanol, methane, formaldehyde etc., can be obtained with the multiple-electron transfer involved during CO₂ electrochemical reduction. Consequently, the selectivity of the target products can be usually low because of the close redox potentials of different reaction

pathways [8–11]. Therefore, development of appropriate catalysts to lower the kinetic energy barriers and steer the selectivity is the primary challenge in the field of ECR [12–15]. Moreover, the hydrogen evolution reaction (HER), as a great competitor, can easily occur at a similar thermodynamic potential than that of CO₂ reduction in aqueous electrolytes [16,17].

Formate is a common organic chemical materials widely used in industries such as pesticide, leather, dye, medicine and rubber. The energy-storing reaction for CO₂ conversion to formate involved two electrons transfer process can be expressed as follows [18–20].



Of all catalysts investigated up to date, the heavy metals (e.g., Pb, Hg, In, Sn and Cd) have documented significant catalytic activity and selectivity for the ECR towards formate [21–24]. Especially, the non-toxic and low-cost Sn has shown its prospect for the ECR towards formate of high Faradaic efficiency (> 90%) [25]. Nevertheless, a low energy conversion efficiency was commonly observed in this type of catalyst due to a high overpotential (η) and a low exchange current

* Corresponding author.

E-mail address: ciac_sheny@mail.hust.edu.cn (Y. Shen).

<https://doi.org/10.1016/j.apcatb.2019.118040>

Received 8 May 2019; Received in revised form 16 July 2019; Accepted 1 August 2019

Available online 02 August 2019

0926-3373/ © 2019 Published by Elsevier B.V.

density (I_0). Instability is another issue for Sn-based catalysts before practical application [26–29]. The high η might be derived from a weak binding interaction among reaction intermediates and catalysts. The low I_0 can result from the slow electron transfer kinetics [30,31]. Several experimental results and computation investigations have suggested that the electronic structure of Sn-based catalysts and their morphology play a critical role in their electrochemical performance [32–36]. This can be correlated with an increase of catalytic active sites and a decrease of the binding energies for reaction intermediates (*CO or CO_2^{*}) on these active featured sites. For example, a nano-porous Sn foam electrode featuring of high surface area and porous structure was developed for the generation of formate with high activity and selectivity [37]. Moreover, the presence of SnO_x was reported to contribute to the stabilized CO_2^{*} intermediate and thus enhance the current density and Faradaic efficiency for CO_2 reduction [38]. In addition, by carefully tuning the surface electronic configuration of the Sn alloys with Pd, Sn, and O, the catalytic activity and selectivity can be significantly improved [39]. Clearly, the structural regulation of heterogeneous atoms can principally improve the Sn-based catalysts for CO_2 electrochemical performance.

As heterogeneous electrocatalysis essentially occurs at the electrode/electrolyte interface, the catalyst surface plays a key role in determining the reactant adsorption and electron transfer processes, and in turn, tailor the catalytic activity and selectivity. Keeping above viewpoints in mind, we designed and synthesized embedded Sn-Cu bimetallic catalyst with electronic structure regulation of atomic Sn by electrochemical deposition heterogeneous atomic Cu for the highly efficient and stable ECR purpose. Cu has been suggested to possess similar catalytic activity to Sn metal for the ECR from experimental and theoretical investigations [25,40,41]. We found that the embedded Sn-Cu bimetallic catalyst exhibited high selectivity and activity for formate production with a Faradaic efficiency of 92% at -0.95 V (vs. RHE) in CO_2 saturated 0.1 M KHCO_3 aqueous solution. Even more encouragingly, the Sn-Cu bimetallic electrodes showed stable ECR capability during 12 h continuous electrolysis.

2. Experimental section

2.1. Synthesis of bimetallic catalyst

The copper foil (Cu foil) is the substrate for electrocatalyst. Electropolishing is a well-known technique that removes material from a metallic workpiece, reducing the surface roughness by leveling micro-peaks and valleys, improving the surface finish. So, Cu foil (approximately $1\text{ cm} \times 2.5\text{ cm}$) was treated with electropolishing in 85% phosphoric acid at an applied bias at 4.0 V for 5 min, and subsequently rinsed with great amount deionized (DI) water and dried by N_2 . The imbedded structure bimetallic Sn-Cu catalyst (BM Sn-Cu) was electrochemically synthesized by a two-step process. Firstly, it carried out potentiostatically in 10 mM SnCl_2 and 0.1 M KCl mixture aqueous solution at -0.6 V vs. Ag/AgCl for 7 min at room temperature and was rinsed with DI water and dried by N_2 , thus Sn nanoparticle formed on substrate. Then the containing Sn nanoparticles substrate was carried out potentiostatically in 10 mM CuCl_2 and 0.1 M KCl mixture aqueous solution through under-potential deposition, thus Cu formed embedded in Sn nanoparticles. The deposition potential of Cu was determined according to CV curve. The electrochemical deposition was conducted in a standard three electrode system with a working electrode, an Ag/AgCl reference electrode and a platinum counter electrode.

2.2. Electrochemical measurement

N_2 was bubbled into the electrolyte for 30 min (pH 8.2) before all the electrochemical measurement. The reduction of CO_2 was performed in CO_2 saturated electrolyte under room temperature and ambient pressure. Prior to the experiments, the solution was bubbled with CO_2

for 30 min (pH 6.8) and then continuously fed into the cathodic chamber during the electrocatalytic reaction process. The electrochemical performance measurements were carried out in a typical H-type cell at room temperature with a 0.1 M KHCO_3 solution on an electrochemical workstation (CHI 660D). The cathode and anode compartments are separated by a proton exchange membrane (Nafion® 117). Platinum wire and a saturated calomel electrode (SCE) were used as the counter and reference electrodes, respectively. The measured potential values (vs. SCE) were converted into those (vs. RHE) according to the Nernst equation. Cyclic voltammetry to study the electrochemical active specific area of the materials were conducted in N_2 -saturated 0.1 M KHCO_3 solution at various scan rates with a potential range where no faradaic process occurs. The electrochemical impedance spectroscopy characterization was measured in a frequency range from 0.1 MHz to 0.01 Hz at a potential of -0.2 V (vs. SCE) with an amplitude of 5 mV.

2.3. Product analysis

The gaseous products were qualitatively analysed using a gas chromatograph (Agilent GC-2020) equipped with a Pora PLOT Q column and a molecular sieve column. The GC configuration contain a flame ionization detector (FID) with methanizer and thermal conductivity detector (TCD), with N_2 carrier gas. The liquid products were analysed by nuclear magnetic resonance (NMR) (Bruker Ascend TM 600 MHz) spectroscopy; for quantifying the liquid products, 400 μL of electrolyte was mixed with 200 μL of D_2O and 100 μL of 5 mM dimethyl sulfoxide (DMSO, 99.99%) as an internal standard. The ^1H spectrum was measured with water suppression using a pre-saturation method. Faraday efficiency is calculated (for the liquid products) according to following equation.

$$\text{FE}_{\text{HCOOH}} = \frac{2nF}{Q} \times 100\% \quad (2)$$

Where n is the yield of HCOOH (mol), F is the faraday constant ($96,485\text{ C mol}^{-1}$), Q is the electric quantity of reaction consumption (C).

The turnover frequency (TOF, s^{-1}) of HCOOH was calculated according to following equation:

$$\text{TOF} = \frac{J_{\text{HCOOH}} \times \text{geometric surface area} / nF}{\left(\omega_{\text{Cu}} \times \frac{m_{\text{catalyst}}}{M_{\text{Cu}}} \right) + \left(\omega_{\text{Sn}} \times \frac{m_{\text{catalyst}}}{M_{\text{Sn}}} \right)} \quad (3)$$

Where ω is the content of Cu and Sn in the catalyst (wt%, measured by XPS); m_{catalyst} is the catalyst mass, M_{Sn} and M_{Cu} are the relative atomic mass of Sn and Cu.

3. Results and discussion

In this study, Sn nanoparticles (coded as M Sn) were firstly electrochemically deposited on the pre-treatment polished Cu foils at -0.6 V (vs. SCE). Then, a small amount Cu was further synthesized onto the top of M Sn film, with spontaneously filling the space among Sn nanoparticles to get the embedded bimetallic Sn-Cu (coded as BM Sn-Cu) catalyst by under-potential deposition. The deposition potential for Sn and Cu was determined by CV as shown in Fig. S1. Additionally, to better understand the different chemical conditions of Sn and Cu elements on catalysts performance, we also fabricated metal Cu (M Cu) and thick-Sn covered M Cu (BM Cu-Sn) catalysts using the same deposition parameters. Fig. 1a and Fig. S2 shows the XRD patterns of the polished Cu (i.e., the substrate), M Sn, M Cu, BM Cu-Sn and BM Sn-Cu samples, respectively. The peaks at 43.3° , 50.4° , 74.1° correspond to the (111), (200), (220) planes of Cu substrates. The peaks at 30.6° , 32.0° , 43.8° , 44.9° , 64.5° for M Sn-Cu and M Sn correspond to the (200), (101), (220), (211), (321) planes of Sn, indicating the existence of metallic state Sn. Significantly, the formed Cu-embedded Sn samples ($\sim 20\text{ nm}$, Fig. 1c) obtained by under-potential deposition technique show much

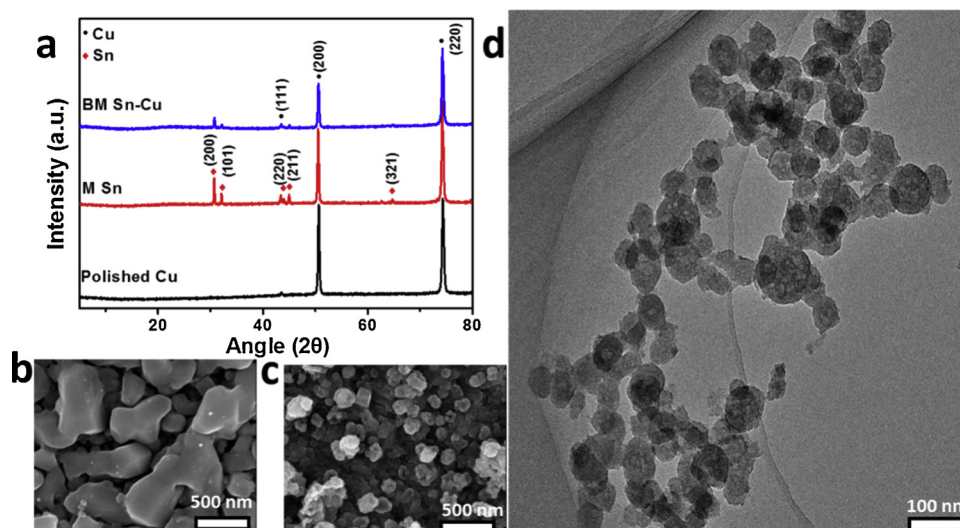


Fig. 1. (a) XRD patterns of Polished Cu, M Sn and BM Sn-Cu; Morphological characterization of the catalysts. (b) Scanning electron micrographs (SEM) of catalysts M Sn; (c) the M Sn after deposition of Cu; (d) Bright-field transmission electron microscope (TEM) image of BM Cu-Sn catalysts.

decreased particles size compared with the precursor Sn samples (~ 500 nm, Fig. 1b). This can be further verified with bright-field TEM characterization in Fig. 1d, showing a uniformly distributed BM Sn-Cu nanoparticles with a size of ~ 20 nm. This dramatic change of morphology which is also a sign of abundant interfaces generation could be caused by grain reorganization and structural optimization during the precious under-potential deposition Cu atoms into Sn layer [42]. The spontaneous insertion of Cu atoms into Sn lattices can be further verified with DFT modelling calculation.

The morphology characterized is further demonstrated by HRTEM on the BM Sn-Cu nanoparticles, featuring with lattice spacing at 0.171 nm and 0.276 nm (Fig. 2a and b). These correspond to the spacing of the (101) plane of Sn and the (200) plane of Cu. Furthermore, a slightly lattice contraction for Sn and Cu was observed as shown in Fig. 2c. This is a result of metal lattice effect between Sn and Cu strong interaction, which indicates a successful insertion of Cu atom into Sn lattice after under-potential deposition technique. The symbiosis of Sn

with Cu elements were further verified by the high-angle annular dark field-STEM (Fig. 2d) and elemental mapping (Fig. 2e and f). Owing to the embedded structure, the Cu element presents a concentrated distribution, accompanied by a marginal distribution of the Sn element.

The electrocatalytic activity of various electrodes were firstly investigated by LSV measurements in N_2 saturated 0.1 M $KHCO_3$ electrolytes in potential ranges from 0 to -1.2 V (vs. RHE) at a scan rate of 20 mV s^{-1} . Owing to the chemical stability of N_2 , the negative current observed from LSV was corresponding to HER. Obviously, the current density was significantly suppressed at the BM Sn-Cu and M Sn electrodes compared to the polished Cu in Fig. 3a, indicating the inactivation of Sn metal for hydrogen evolution reaction. Specifically, at -1.05 V, the cathodic current density of the BM Sn-Cu was about 1.9 mA cm^{-2} , being about one fifth of the polished Cu (10.76 mA cm^{-2}). When CO_2 saturated electrolytes were used, both the BM Sn-Cu and M Sn electrode showed an increased current density, while an ignorable change was found onto the polished Cu electrode (Fig. 3b). In

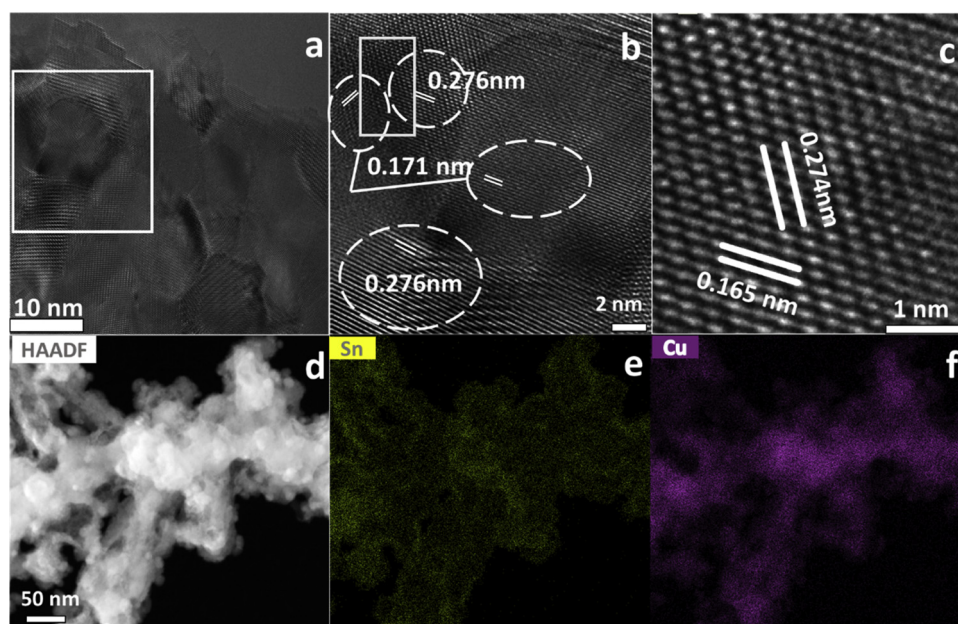


Fig. 2. (a–c) HR-TEM (high resolution) image of BM Sn-Cu catalyst; (d) HAADF (high-angle annular dark field)-STEM; STEM elemental mapping results of BM Sn-Cu catalyst. (e) Sn; (f) Cu.

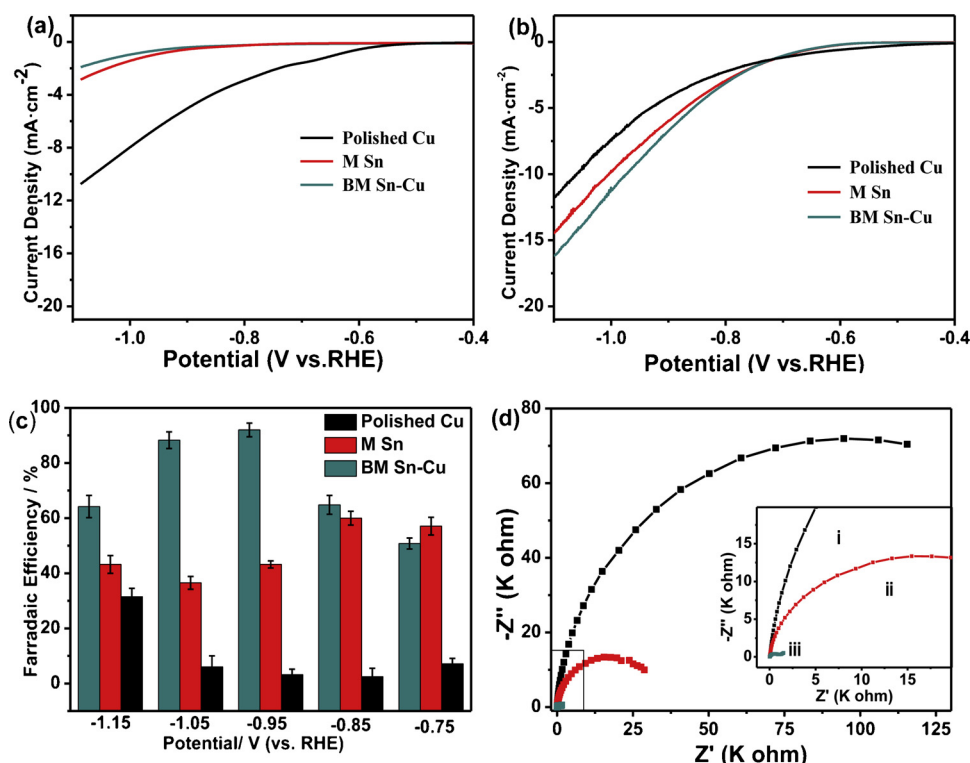


Fig. 3. CO₂ electrochemical reduction performance about Polished Cu, M Sn and BM Sn-Cu. LSV curve in N₂ (a) CO₂ (b) saturated 0.1 M KHCO₃ solutions. (c) Faradaic efficiencies for formate at potential range from -0.75 V to -1.15 V (vs. RHE) in CO₂ saturated 0.1 M KHCO₃ electrolyte. Electrolysis time: 2 h. (d) Nyquist plots of M Sn (i), BM Cu-Sn (ii), BM Sn-Cu (iii) recorded in 0.1 M KHCO₃ solution.

combination with the similar phenomenon observed on the BM Cu-Sn electrode (Fig. S3), we proposed that Sn plays a key role for the high selectivity for ECR performance in the bimetallic catalysts. NMR measurement confirmed formate as the major liquid product at an applied potentials ranging from -0.75 V to -1.15 V (vs. RHE). Fig. 3c compares the Faradaic efficiency of formate for the polished Cu, M Sn and BM Sn-Cu electrodes. The BM Sn-Cu electrode showed the higher Faradaic efficiency (being 92% at -0.95 V) for the formate formation than most of Cu or Sn electrodes, while the total Faradaic efficiency of gas products (H₂ and CO) is less than 10% on the BM Sn-Cu electrode. The Faradaic efficiency for the formate formation decreased when the potential was negatively shifted. This can be ascribed to an increased competitive hydrogen evolution reaction, which was also reflected by bubbles nearby electrode surface. Fig. S4 compares the Faradaic efficiencies for ECR to formate on the M Cu, M Cu-Sn catalysts and Fig. S5 shows the Faradaic efficiencies for ECR to H₂ and CO on the all mentioned catalysts. In terms of formate production, the bimetallic catalyst are superior to that of single metal with an order of BM Sn-Cu > BM Cu-Sn > M Sn > M Cu > the polished Cu (Table S1). To the best of our knowledge, among the reported Sn or Cu catalysts for ECR to produce formate, the BM Sn-Cu catalysts achieves the superior Faradaic efficiency and the current density (Table S2). To probe the influence of active sites, we measured the electrochemical active specific area (ECSA) of the catalysts based on the double layer capacitances (Fig. S6). The capacitances for BM Sn-Cu was about $310.5 \mu\text{F cm}^{-2}$, which is about three times and five times enhancement compared with that for the BM Cu-Sn ($113.2 \mu\text{F cm}^{-2}$) and that for the M Sn ($63.4 \mu\text{F cm}^{-2}$) respectively. This result implied that the embedded structure of BM Sn-Cu can supply more active sites for CO₂ reduction. We further studied the interfacial charge transfer process for electrocatalysts in the electrolyte was further studied with electrochemical impedance measurement. In Fig. 3d, the BM Sn-Cu (curve iii) showed the smallest diameter of the semicircle than that of M Sn and BM Cu-Sn. Generally speaking, the diameter of the semicircle in Nyquist plots is typical of the interfacial charge transfer resistance (R_{ct}) across the electrode/electrolyte interface. A smaller diameter indicates faster electron transfer reaction on the interface between electrode and electrolyte. The detailed

analysis of impedance characterization and fitting equivalent circuit are shown in Fig. S7 and Table S3. Specifically, a reduced R_{CT-1} and R_{CT-2} on the BM Sn-Cu electrode, which represent the charge-transfer resistance at the substrate/electrocatalyst film and electrocatalyst film/electrolyte interface, could be correlated to the embedded structure. The abundant heterogeneous interfaces can offer more channels and shorter path for electron transfer and thus speed up the electron transportation. This conclusion agrees well with the Tafel slope and TOF measurements. The Tafel slope of the BM Sn-Cu, BM Cu-Sn and M Sn electrodes were measured to be 104, 123 and 128 mV dec^{-1} , respectively (Fig. S9a). The lower Tafel slope of the BM Sn-Cu electrode indicates a faster electrode reaction [43,44]. The TOF of BM Sn-Cu was 0.009 s^{-1} with the potential of -1.0 V, while the BM Cu-Sn was 0.007 s^{-1} , the M Sn was 0.0029 s^{-1} . We further tested the durability of BM Sn-Cu electrode at multiple potentials. During the measurement, CO₂ gas was kept bubbling in electrolytes to maintain an uninterrupted supply and buffer the change of pH. As shown in Fig. S9b, the BM Sn-Cu showed constant current during an electrolysis experiment for 12 h with potentials ranging from -0.75 V to -0.95 V. The corresponding Faradaic efficiency for formate production retained stable at 40.7% (-0.75 V), 60.1% (-0.85 V) and 90.4% (-0.95 V)."

It's well known that the electronic structure of catalyst plays a vital role in the electrocatalytic activity. X-ray photoelectron spectroscopy (XPS) characterization was conducted to measure the chemical states of the M Sn, BM Cu-Sn, and BM Sn-Cu samples. Fig. 4a shows the high-resolution Cu 2p spectra of these three catalyst samples. The two main peaks with binding energies of 932.7 eV and 952.6 eV can be assigned to the Cu 2p_{3/2} and Cu 2p_{1/2} peaks of metallic state Cu⁰, respectively. Since the peak at 943.9 eV can hardly differentiate Cu⁺ from Cu⁰, it is necessary to analyze Cu LM2 auger spectrum. As shown in Fig. S8, the peak at 918.6 eV is ascribed to Cu⁰, and the distinctively peak at 916.9 eV on BM Sn-Cu is coinciding with the standard auger spectrum of Cu₂O [45], which further confirm the generation of Cu₂O during under-potential deposition Cu onto the Sn surface compared with BM Cu-Sn and M Sn. Fig. 4b shows the detailed XPS spectra of Sn 3d_{5/2} and Sn 3d_{3/2} of metallic state Sn⁰ and inevitable metal oxidation SnO₂. The binding energy for Sn (IV) in the BM Cu-Sn and BM Sn-Cu samples

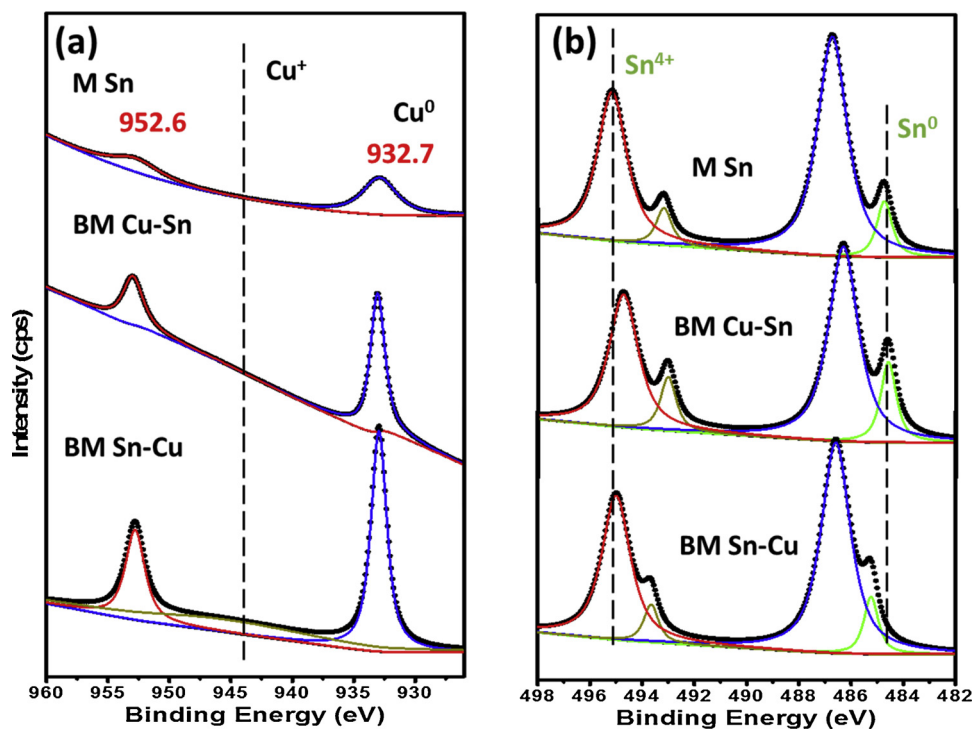


Fig. 4. (a) Cu 2p XPS spectral and (b) Sn 3d XPS spectral of M Sn, BM Cu-Sn, and BM Sn-Cu catalysts.

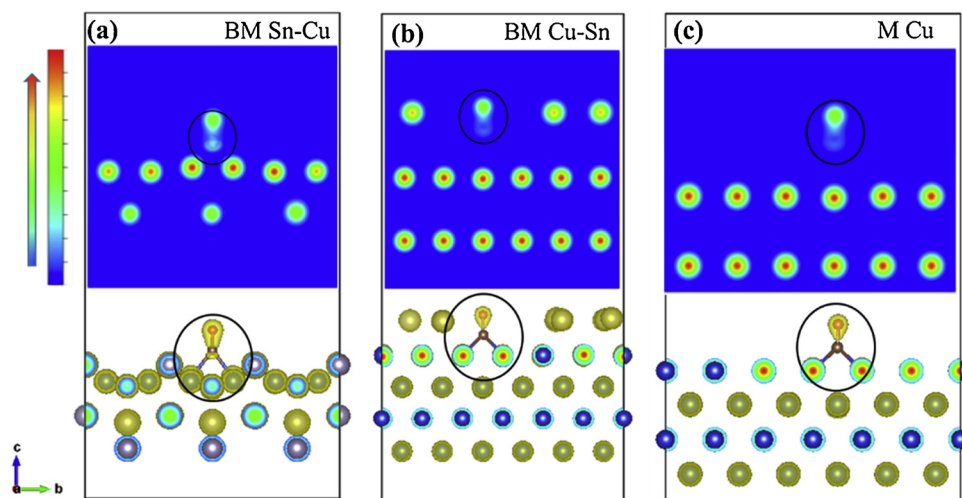


Fig. 5. The three-dimensional and two-dimensional diagrams about simulated result of the electron density distribution in the (a) BM Sn-Cu, (b) BM Cu-Sn and (c) M Cu catalyst models after adsorption of CO_2 via the C atoms. (The color changing from blue to red means an increasing of electron on the two-dimensional diagrams). (For interpretation of the references to colour in this figure legend, the reader is referred to the web version of this article).

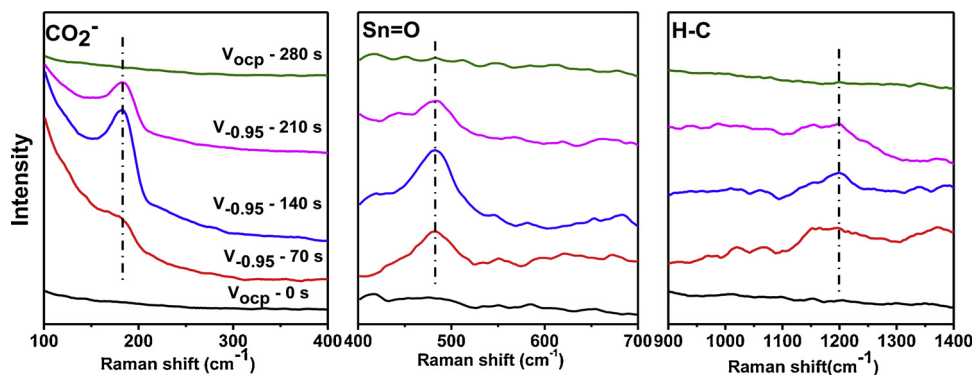


Fig. 6. In-situ Raman spectra with the BM Sn-Cu electrode reaction at -0.95 V (vs. RHE) or without reaction in CO_2 saturated 0.1 M KHCO_3 solutions.

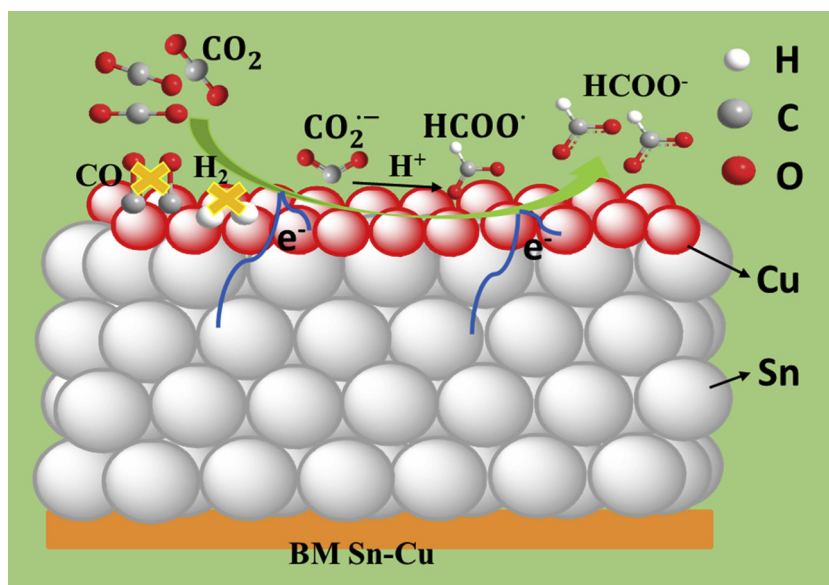


Fig. 7. Proposed reaction mechanism for electrochemical reduction of CO₂ to formate at BM Sn-Cu electrode.

negative shifts compared to the M Sn, which might be due to the surface effect (an increase in the ratio of surface/bulk atoms in the nano sized particles) correlated with the composition of Cu [46,47]. Remarkably, the binding energy for the Sn⁰ (~484.7 eV and ~493.1 eV) in the sample of BM Sn-Cu positively shifts compared to the M Sn and the BM Cu-Sn samples. The clearly positive shift binding energy of the Sn⁰ indicates a decrease of Fermi level on the valence band of 3d orbit (*i.e.*, a lower electron density) on Sn metal. Therefore, CO₂ will prefer to be chemically adsorbed on atomic Sn of the bimetallic catalyst due to lone pair electrons from O atoms of CO₂, and thus accelerate the CO₂ reduction reaction [48,49].

We further performed density functional calculations to understand the electronic structure of the embedded bimetallic Sn-Cu for ECR. Fig. S10 shows the computational modelling of BM Sn-Cu, and BM Cu-Sn catalysts. After lattice optimization the BM Sn-Cu model presents an embedded structure. The adsorption capacities of key intermediates (*H and *CO) are determined for the evolution of CO₂ reduction performance [25,50]. Herein, we especially compared the adsorption energy for *H and *CO onto the ideal M Cu (2.50/1.07 eV), BM Cu-Sn (3.49/2.19 eV), and BM Sn-Cu (3.74/3.3 eV) samples (Table S4). The calculated adsorption energy for the *H and *CO onto the surface of BM Sn-Cu was higher than that of M Cu and BM Cu-Sn catalysts. As well known, a strong adsorption of *H and *CO can relatively hinder desorption of the possible products H₂ and CO from electrocatalyst. Moreover, Table S4 shows the adsorption energy of *HCOO onto the M Sn (3.55 eV), BM Cu-Sn (4.37 eV) and BM Sn-Cu (1.36 eV), which is the key intermediate for formate. Less energy for adsorption indicates easier desorption for the intermediate *HCOO. This is critical for formate generation. Consequently, we observed high selectivity for formate on the BM Sn-Cu electrode with less than 10% production of H₂ and CO. To explore charge-transfer between reactant and electrode surface, we further simulated the charge distribution of the M Cu, BM Cu-Sn and BM Sn-Cu after CO₂ adsorption as presented in Fig. 5 (a-c). The gradient of color from blue to red indicates the increasing of electrons density. Clearly, the electron density of CO₂ at the surface of BM Sn-Cu is higher than those of M Cu and BM Cu-Sn, which is correlating with the amount of charge-transfer from electrode surface to CO₂. It indicates that the embedded structure of BM Sn-Cu enables a more charge-transfer during CO₂ reduction reaction. DFT calculation indicates a high possibility of attachment of CO₂ to the Cu atoms during the reduction process. The information of calculation is presented in the supporting information (Figs. S11, S12 and Table S5). Herein, the

bridge of Cu atoms plays a key role in the ECR via promoting the electron-transfer.

In-situ Raman spectroscopy characterization was further carried out to identify the intermediates during the reduction process. The Raman signals were recorded at open circuit potential condition (V_{OCP})-0 s, an applied potential (-0.95 V) $V_{-0.95}$ -70 s, $V_{-0.95}$ -140 s, $V_{-0.95}$ -210 s, and V_{OCP} -280 s on the BM Sn-Cu electrode in CO₂ saturated 0.1 M KHCO₃ solution and the results are shown in Fig. 6. The in-situ Raman spectroscopy signal originates from the emergence of intermediates. These signals vanished after stopping applied potential. The peaks near 180 cm⁻¹ and 1197 cm⁻¹ in Fig. 6 correspond to vibrational modes of CO₂^{•-} and H-C [51]. The appeared peak at 480 cm⁻¹ corresponds to the vibration signal of Sn=O [52]. We also carried out the in-situ Raman spectroscopy measurements with the BM Sn-Cu electrode at different voltages (Fig. S13). The CO₂^{•-} and Sn=O peak intensity increases as potential increasing from -0.75 to -1.05 V (vs. RHE). It can be inferred that CO₂^{•-} and HCOO⁻ are the intermediates occurring in the reaction. Moreover, the other information is that the intermediates (CO₂^{•-}) can attach with Sn via the O atom, which is consistent with electron structure analysis about Sn XPS spectra. Since the XPS analysis has proved the existence of SnO₂ (namely Sn=O) in the BM Sn-Cu catalyst, it is necessary to identify the origination of Sn=O signals in the in-situ Raman results. We further carried out the ex-situ Raman spectroscopy characterization to verify the Sn=O signal during the reduction reaction. As shown in Fig. S14, there are no signals at the Raman shift in M Sn, BM Cu-Sn and BM Sn-Cu. This result could be corrected to the strength of Sn=O signal, which becomes stronger during the reduction process.

In combination with the observation from DFT calculations, we propose the CO₂ reduction process to formate in the embedded bimetallic catalyst as following: (i) chemical adsorption of CO₂ on the embedded structure BM Sn-Cu catalyst in the form of Sn-O and Cu-C attachment; (ii) first electron transfers from the Sn or Cu atoms to CO₂, resulting C=O bonds broken to form CO₂^{•-} and proton migration to form C-H bonds (HCOO⁻); (iii) configuration rearrangement of HCOO⁻ by obtaining a secondary electron; (iv) desorption from the bimetallic catalyst surface and diffusion into electrolytes. Consequently, the reaction mechanism for electrochemical reduction of CO₂ to formate at the BM Sn-Cu electrode can be illustrated in Fig. 7 [29,53].

4. Conclusion

In summary, we have successfully demonstrated an embedded Sn-Cu bimetallic catalyst for efficient electrochemical reduction of CO₂ to formate. The formed Sn-Cu catalyst showed a high Faradaic efficiency of 92% for formate production at the applied potential of -0.95 (vs. RHE) in a CO₂-saturated 0.1 M KHCO₃ solution with a sustainable selectivity and stability over 12 h. The existence of intermediates CO₂^{•−} and HCOO[•] confirmed by in-situ Raman spectroscopy characterization and DFT calculation suggests the reaction pathway on the embedded bimetallic catalyst contains two-step procedure from CO₂ to CO₂^{•−} and CO₂^{•−} to HCOO[•] (ads) on CO₂ reduction to formate. An imbedded Sn-Cu bimetallic catalyst can not only generate abundant interfaces, but also regulate electronic structure to accelerate the process of CO₂ reduction. This research could open up a new way for heterogeneous metal catalysts to regulate electronic structure toward efficient CO₂ reduction.

Declaration of Competing Interest

The authors declare that they have no known competing financial interests or personal relationships that could have appeared to influence the work reported in this paper.

Acknowledgements

This work was financially supported from the NSFC Major International (Regional) Joint Research Project NSFC-SNSF (51661135023), NSFC (21673091), the Fundamental Research Funds for the Central Universities (HUST: 2016YXMS031), China Postdoctoral Science Foundation funded project (2018M632823), the Director Fund of the WNLO, and the Open Funds of the State Key Laboratory of Electroanalytical Chemistry (SKLEAC201607). The authors thank the Analytical and Testing Center of HUST and the Center of Micro-Fabrication and Characterization of WNLO for the measurements. Thanks to the facility support of the Center for Nanoscale Characterization & Devices (CNCD), WNLO of HUST.

Appendix A. Supplementary data

Supplementary material related to this article can be found, in the online version, at doi:<https://doi.org/10.1016/j.apcatb.2019.118040>.

References

- [1] H.-R.M. Jhong, S. Ma, P.J.A. Kenis, Electrochemical conversion of CO₂ to useful chemicals: current status, remaining challenges, and future opportunities, *Curr. Opin. Chem. Eng.* 2 (2013) 191–199.
- [2] K.-H. Liu, H.-X. Zhong, S.-J. Li, Y.-X. Duan, M.-M. Shi, X.-B. Zhang, J.-M. Yan, Q. Jiang, Advanced catalysts for sustainable hydrogen generation and storage via hydrogen evolution and carbon dioxide/nitrogen reduction reactions, *Prog. Mater. Sci.* 92 (2018) 64–111.
- [3] K.-H. Liu, H.-X. Zhong, X.-Y. Yang, D. Bao, F.-L. Meng, J.-M. Yan, X.-B. Zhang, Composition-tunable synthesis of “clean” syngas via a one-step synthesis of metal-free pyridinic-N-enriched self-supported CNTs: the synergy of electrocatalyst pyrolysis temperature and potential, *Green Chem.* 19 (2017) 4284–4288.
- [4] D.T. Whipple, P.J. Kenis, Prospects of CO₂ utilization via direct heterogeneous electrochemical reduction, *J. Phys. Chem. Lett.* 1 (2010) 3451–3458.
- [5] A. Aylmer-Kelly, A. Bewick, P. Cantrill, A. Tuxford, Studies of electrochemically generated reaction intermediates using modulated specular reflectance spectroscopy, *Faraday Discuss. Chem. Soc.* 56 (1973) 96–107.
- [6] E. Lamy, L. Nadjo, J. Saveant, Standard potential and kinetic parameters of the electrochemical reduction of carbon dioxide in dimethylformamide, *J. Electron. Chem. Interface Electrochem.* 78 (1977) 403–407.
- [7] H. Schwarz, R. Dodson, Reduction potentials of CO₂-and the alcohol radicals, *J. Phys. Chem.* 93 (1989) 409–414.
- [8] K.P. Kuhl, E.R. Cave, D.N. Abram, T.F. Jaramillo, New insights into the electrochemical reduction of carbon dioxide on metallic copper surfaces, *Energy Environ. Sci.* 5 (2012) 7050–7059.
- [9] Y. Hori, A. Murata, R. Takahashi, Formation of hydrocarbons in the electrochemical reduction of carbon dioxide at a copper electrode in aqueous solution, *J. Chem. Soc. Faraday Trans 1* (85) (1989) 2309–2326.
- [10] R. Kortlever, J. Shen, K.J.P. Schouten, F. Calle-Vallejo, M.T.M. Koper, Catalysts and reaction pathways for the electrochemical reduction of carbon dioxide, *J. Phys. Chem. Lett.* 6 (2015) 4073–4082.
- [11] D. Bao, Q. Zhang, F.L. Meng, H.X. Zhong, M.M. Shi, Y. Zhang, J.M. Yan, Q. Jiang, X.B. Zhang, Electrochemical reduction of N₂ under ambient conditions for artificial N₂ fixation and renewable energy storage using N₂/NH₃ cycle, *Adv. Mater.* 29 (2017) 1604799.
- [12] J. Liu, C. Guo, A. Vasileff, S. Qiao, Nanostructured 2D materials: prospective catalysts for electrochemical CO₂ reduction, *Small Methods* 1 (2017) 1600006.
- [13] Z. Sun, T. Ma, H. Tao, Q. Fan, B. Han, Fundamentals and challenges of electrochemical CO₂ reduction using two-dimensional materials, *Chemistry* 3 (2017) 560–587.
- [14] A. Vasileff, Y. Zheng, S.Z. Qiao, Carbon solving carbon's problems: recent progress of nanostructured carbon-based catalysts for the electrochemical reduction of CO₂, *Adv. Energy Mater.* 7 (2017) 1700759.
- [15] L. Zhang, Z.-J. Zhao, J. Gong, Nanostructured materials for heterogeneous electrocatalytic CO₂ reduction and their related reaction mechanisms, *Angew. Chem. Int. Ed. English* 56 (2017) 11326–11353.
- [16] Y. Hori, Electrochemical CO₂ reduction on metal electrodes, in: C.G. Vayenas, R.E. White, M.E. Gamboa-Aldeco (Eds.), *Modern Aspects of Electrochemistry*, Springer, New York, New York, NY, 2008, pp. 89–189.
- [17] H.-x. Zhong, K. Li, Q. Zhang, J. Wang, F.-l. Meng, Z.-j. Wu, J.-m. Yan, X.-b. Zhang, In situ anchoring of Co 9 S 8 nanoparticles on N and S co-doped porous carbon tube as bifunctional oxygen electrocatalysts, *NPG Asia Mater.* 8 (2016) e308.
- [18] Q. Lu, F. Jiao, Electrochemical CO₂ reduction: electrocatalyst, reaction mechanism, and process engineering, *Nano Energy* 29 (2016) 439–456.
- [19] X. Li, J. Wen, J. Low, Y. Fang, J. Yu, Design and fabrication of semiconductor photocatalyst for photocatalytic reduction of CO₂ to solar fuel, *Sci. China Mater.* 57 (2014) 70–100.
- [20] R. Chaplin, A. Wragg, Effects of process conditions and electrode material on reaction pathways for carbon dioxide electroreduction with particular reference to formate formation, *J. Appl. Electrochem.* 33 (2003) 1107–1123.
- [21] Z. Chen, N. Wang, S. Yao, L. Liu, The flaky Cd film on Cu plate substrate: an active and efficient electrode for electrochemical reduction of CO₂ to formate, *J. CO₂ Util.* 22 (2017) 191–196.
- [22] Z.-L. Wang, C. Li, Y. Yamauchi, Nanostructured nonprecious metal catalysts for electrochemical reduction of carbon dioxide, *Nano Today* 11 (2016) 373–391.
- [23] L. Sun, G.K. Ramesha, P.V. Kamat, J.F. Brennecke, Switching the reaction course of electrochemical CO₂ reduction with ionic liquids, *Langmuir* 30 (2014) 6302–6308.
- [24] Z.M. Detweiler, J.L. White, S.L. Bernasek, A.B. Bocarsly, Anodized indium metal electrodes for enhanced carbon dioxide reduction in aqueous electrolyte, *Langmuir* 30 (2014) 7593–7600.
- [25] J.T. Feaster, C. Shi, E.R. Cave, T. Hatsukade, D.N. Abram, K.P. Kuhl, C. Hahn, J.K. Nørskov, T.F. Jaramillo, Understanding selectivity for the electrochemical reduction of carbon dioxide to formic acid and carbon monoxide on metal electrodes, *ACS Catal.* 7 (2017) 4822–4827.
- [26] A.S. Agarwal, Y. Zhai, D. Hill, N. Sridhar, The electrochemical reduction of carbon dioxide to formate/formic acid: engineering and economic feasibility, *ChemSusChem* 4 (2011) 1301–1310.
- [27] C. Oloman, H. Li, Electrochemical processing of carbon dioxide, *ChemSusChem* 1 (2008) 385–391.
- [28] J. Wu, F. Risalvato, X.-D. Zhou, Effects of the electrolyte on electrochemical reduction of CO₂ on Sn electrode, *ECS Trans.* 41 (2012) 49–60.
- [29] S. Zhang, P. Kang, T.J. Meyer, Nanostructured tin catalysts for selective electrochemical reduction of carbon dioxide to formate, *J. Am. Chem. Soc.* 136 (2014) 1734–1737.
- [30] F. Li, L. Chen, G.P. Knowles, D.R. MacFarlane, J. Zhang, Hierarchical mesoporous SnO₂ nanosheets on carbon cloth: a robust and flexible electrocatalyst for CO₂ reduction with high efficiency and selectivity, *Angew. Chem. Int. Ed.* 56 (2017) 505–509.
- [31] Y. Li, F. Cui, M.B. Ross, D. Kim, Y. Sun, P. Yang, Structure-sensitive CO₂ electroreduction to hydrocarbons on ultrathin 5-fold twinned copper nanowires, *Nano Lett.* 17 (2017) 1312–1317.
- [32] S. Back, M.S. Yeom, Y. Jung, Active sites of Au and Ag nanoparticle catalysts for CO₂ electroreduction to CO, *ACS Catal.* 5 (2015) 5089–5096.
- [33] Y.-X. Duan, F.-L. Meng, K.-H. Liu, S.-S. Yi, S.-J. Li, J.-M. Yan, Q. Jiang, Amorphizing of Cu nanoparticles toward highly efficient and robust electrocatalyst for CO₂ reduction to liquid fuels with high faradaic efficiencies, *Adv. Mater.* 30 (2018) 1706194.
- [34] X. Feng, K. Jiang, S. Fan, M.W. Kanan, Grain-boundary-dependent CO₂ electroreduction activity, *J. Am. Chem. Soc.* 137 (2015) 4606–4609.
- [35] W. Zhu, L. Zhang, P. Yang, X. Chang, H. Dong, A. Li, C. Hu, Z. Huang, Z.-J. Zhao, J. Gong, Morphological and compositional design of Pd-Cu bimetallic nanocatalysts with controllable product selectivity toward CO₂ electroreduction, *Small* 14 (2018) 1703314.
- [36] S. Liu, H. Tao, L. Zeng, Q. Liu, Z. Xu, Q. Liu, J.-L. Luo, Shape-dependent electrocatalytic reduction of CO₂ to CO on triangular silver nanoplates, *J. Am. Chem. Soc.* 139 (2017) 2160–2163.
- [37] D. Du, R. Lan, J. Humphreys, S. Sengodan, K. Xie, H. Wang, S. Tao, Achieving both high selectivity and current density for CO₂ reduction to formate on nanoporous tin foam electrocatalysts, *ChemistrySelect* 1 (2016) 1711–1715.
- [38] Y. Chen, M.W. Kanan, Tin oxide dependence of the CO₂ reduction efficiency on tin electrodes and enhanced activity for tin/tin oxide thin-film catalysts, *J. Am. Chem. Soc.* 134 (2012) 1986–1989.
- [39] X. Bai, W. Chen, C. Zhao, S. Li, Y. Song, R. Ge, W. Wei, Y. Sun, Exclusive formation of formic acid from CO₂ electroreduction by tunable Pd-Sn alloy, *Angew. Chem.*

- 129 (2017) 12387–12391.
- [40] S. Sarfraz, A.T. Garcia-Esparza, A. Jedidi, L. Cavallo, K. Takanabe, Cu–Sn bimetallic catalyst for selective aqueous electroreduction of CO₂ to CO, *ACS Catal.* 6 (2016) 2842–2851.
- [41] Y. Zhao, C. Wang, G.G. Wallace, Tin nanoparticles decorated copper oxide nanowires for selective electrochemical reduction of aqueous CO₂ to CO, *J. Mater. Chem. A* 4 (2016) 10710–10718.
- [42] E. Herrero, L.J. Buller, H.D. Abruña, Underpotential deposition at single crystal surfaces of Au, Pt, Ag and other materials, *Chem. Rev.* 101 (2001) 1897–1930.
- [43] W. Luc, C. Collins, S. Wang, H. Xin, K. He, Y. Kang, F. Jiao, Ag–Sn bimetallic catalyst with a core–shell structure for CO₂ reduction, *J. Am. Chem. Soc.* 139 (2017) 1885–1893.
- [44] F. Meng, H. Zhong, J. Yan, X. Zhang, Iron-chelated hydrogel-derived bifunctional oxygen electrocatalyst for high-performance rechargeable Zn–air batteries, *Nano Res.* 10 (2017) 4436–4447.
- [45] G.-F. Pan, S.-B. Fan, J. Liang, Y.-X. Liu, Z.-Y. Tian, CVD synthesis of Cu₂O films for catalytic application, *RSC Adv.* 5 (2015) 42477–42481.
- [46] A. Fernandez, A. Caballero, A. Gonzalez-Elipe, Size and Support Effects in the Photoelectron Spectra of Small TiO₂ Particles, (1992).
- [47] S. Peters, S. Peredkov, M. Neeb, W. Eberhardt, M. Al-Hada, Size-dependent XPS spectra of small supported Au-clusters, *Surf. Sci.* 608 (2013) 129–134.
- [48] D. Huang, B. Zhang, Y. Zhang, F. Zhan, X. Xu, Y. Shen, M. Wang, Electrochemically reduced graphene oxide multilayer films as metal-free electrocatalysts for oxygen reduction, *J. Mater. Chem. A* 1 (2013) 1415–1420.
- [49] F.-L. Meng, Z.-L. Wang, H.-X. Zhong, J. Wang, J.-M. Yan, X.-B. Zhang, Reactive multifunctional template-induced preparation of Fe-N-doped mesoporous carbon microspheres towards highly efficient electrocatalysts for oxygen reduction, *Adv. Mater.* 28 (2016) 7948–7955.
- [50] J.P. Jones, G. Prakash, G.A. Olah, Electrochemical CO₂ reduction: recent advances and current trends, *Isr. J. Chem.* 54 (2014) 1451–1466.
- [51] I.H. Boyaci, H.T. Temiz, H.E. Geniş, E. Acar Soykut, N.N. Yazgan, B. Güven, R.S. Uysal, A.G. Bozkurt, K. İlaslan, O. Torun, F.C. Dudak Şeker, Dispersive and FT-Raman spectroscopic methods in food analysis, *RSC Adv.* 5 (2015) 56606–56624.
- [52] B. Eifert, M. Becker, C.T. Reindl, M. Giar, L. Zheng, A. Polity, Y. He, C. Heiliger, P.J. Klar, Raman studies of the intermediate tin-oxide phase, *Phys. Rev. B Condens. Matter Mater. Phys.* 1 (2017) 014602.
- [53] C. Zhao, J. Wang, Electrochemical reduction of CO₂ to formate in aqueous solution using electro-deposited Sn catalysts, *Chem. Eng. J.* 293 (2016) 161–170.